

# Numerical Simulation and Experimental Validation of Blood Flow in Arteries with Structured-Tree Outflow Conditions

METTE S. OLUFSEN

Department of Mathematics and Center for BioDynamics, Boston University, 111 Cummington Street, Boston, Massachusetts

CHARLES S. PESKIN

Courant Institute of Mathematical Sciences, New York University, 251 Mercer Street, New York, New York

WON YONG KIM and ERIK M. PEDERSEN

Department of Cardiothoracic and Vascular Surgery and MR-Center, Institute for Experimental and Clinical Research, Skejby Sygehus, Aarhus University Hospital, 8200 Aarhus N, Denmark

ALI NADIM

Department of Aerospace and Mechanical Engineering and Center for BioDynamics, Boston University, 110 Cummington Street, Boston, Massachusetts

JESPER LARSEN

Math-Tech Inc, Admiralgade 22, 1066 Copenhagen, Denmark

(Received 11 February 2000; accepted 18 September 2000)

**Abstract**—Blood flow in the large systemic arteries is modeled using one-dimensional equations derived from the axisymmetric Navier–Stokes equations for flow in compliant and tapering vessels. The arterial tree is truncated after the first few generations of large arteries with the remaining small arteries and arterioles providing outflow boundary conditions for the large arteries. By modeling the small arteries and arterioles as a structured tree, a semi-analytical approach based on a linearized version of the governing equations can be used to derive an expression for the root impedance of the structured tree in the frequency domain. In the time domain, this provides the proper outflow boundary condition. The structured tree is a binary asymmetric tree in which the radii of the daughter vessels are scaled linearly with the radius of the parent vessel. Blood flow and pressure in the large vessels are computed as functions of time and axial distance within each of the arteries. Comparison between the simulations and magnetic resonance measurements in the ascending aorta and nine peripheral locations in one individual shows excellent agreement between the two. © 2000 Biomedical Engineering Society. [S0090-6964(00)00311-8]

**Keywords**—Arterial blood flow, Arterial modeling, Blood flow modeling, Arterial outflow conditions, Biofluid dynamics, Mathematical modeling.

---

Address correspondence to Mette S. Olufsen, Department of Mathematics and Center for BioDynamics, Boston University, 111 Cummington St., Boston, MA 02215. Electronic mail: mette@bu.edu

## INTRODUCTION

The aim of this work is to develop and use a one-dimensional fluid-dynamical model predicting blood flow and pressure in the systemic arteries at any position along the vessels. Such a model can be used to study the profile of the flow and pressure waves as they propagate along the arteries. The form of the waves change as a result of the arteries changing geometry and structure.<sup>19,25</sup>

The systemic arteries are compliant vessels which taper along their length and become stiffer with smaller radii. They are organized in a bifurcating tree in which the cross-sectional area of the vessels expands from approximately 5 cm<sup>2</sup> at the aortic root to approximately 400 cm<sup>2</sup> at the arterioles.<sup>6</sup> The expansion occurs because at each bifurcation the combined cross-sectional area of the daughter vessels is larger than that of the parent vessel, even though the cross-sectional area of each of the daughter vessels is smaller than the area of the parent vessel. Furthermore, at the distal end of the arterial tree, at the arteriolar level, there is a high resistance to the flow.<sup>10</sup> As a result, the flow and pressure waves are reflected, and the reflected waves propagate backward through the arterial tree. For example, the reflected wave

is diminished in some people suffering from diabetes or vascular diseases such as atherosclerosis.<sup>9,16,19</sup> It has also been observed that people with stiffer arteries have a less pronounced reflected wave but increased diastolic and systolic pressures.<sup>3,13,19</sup> The profiles of the flow and pressure waves vary significantly even among healthy people.<sup>10</sup> Hence, being able to construct a model based on measured geometry and a single noninvasive flow measurement in the ascending aorta will enable us to study the wave forms for any given subject. Computed pressure and flow profiles could be used as part of a diagnostic tool. For example, for a given subject, measured pathologic flow profiles could be compared with computed healthy flow profiles. Studies of how the model parameters must change to simulate the measured pathologic flow profiles might lead to a better understanding of the pathologic condition. In addition, computation of flows and pressure profiles could be used in connection with simulators, e.g., in surgical or anesthesia simulators.

In this paper we use the one-dimensional fluid-dynamics model developed earlier<sup>21</sup> for a case study comparing simulated flow and pressure waves with flows obtained using magnetic resonance techniques. The geometry (lengths, inlet and outlet radii) of the vessels is obtained using measured data from one subject and other vessel properties (mainly elasticity of the walls and the peripheral resistances) are based on the previous model<sup>21</sup> but with parameters adjusted to compare with the measured data. In addition, the equation specifying how pressures change from a parent vessel into its daughters has been modified. Finally, in our previous work,<sup>21</sup> the fluid dynamical model was stated but not derived; so we provide a complete derivation of the equations and state the algorithms used to solve them.

The model<sup>21</sup> consists of two parts: The large arteries, in which blood flow and pressure are predicted at any point along the vessels, and the small arteries, in which a relation between flow and pressure yields outflow boundary conditions for the large arteries (see Fig. 1). Blood flow and pressure in the systemic arteries (large and small vessels) are determined using the incompressible axisymmetric Navier–Stokes equations for a Newtonian fluid. The one-dimensional model is obtained by integrating these equations over the cross-sectional area of the vessels.

The tree representing the large arteries originates at the heart and includes one or two generations from the aorta, iliac, and femoral arteries. The geometry of the large vessels (lengths and diameters) mimics the actual geometry of the arteries.<sup>4,25,28</sup> These data are obtained by magnetic resonance techniques. Since we are interested in predicting flow and pressure waves for a given subject, lengths and diameters for all vessels must be faithful to the human arterial tree. However, in order to limit

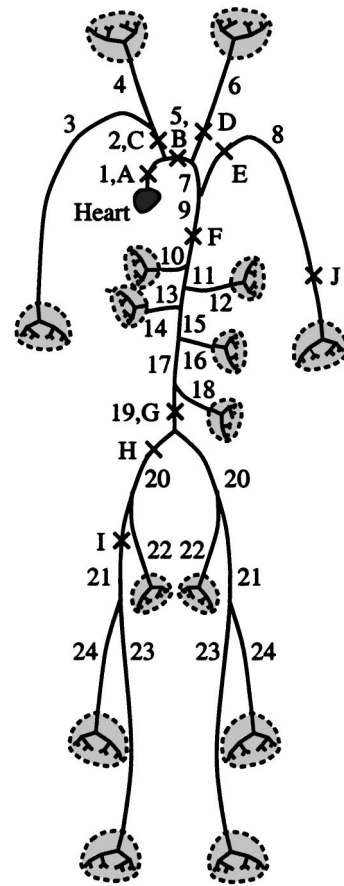


**FIGURE 1.** The systemic arterial tree. The large arteries are modeled as a binary tree where the geometry of the vessels are determined from magnetic resonance measurements. The small arteries are modeled as structured trees attached at the terminals of the large vessels. The geometry of the structured trees does not mimic the actual geometry of the vessels, but is based on general statistical relationships, which are estimated from literature data. The numbers of the vessels refer to the various segments of the large arteries and the dimensions of these segments are given in Table 1. The letters show the ten locations where the flows were measured. The data for these are also specified in Table 1. In order to avoid too many artifacts due to entry region flow, where possible, the flows are measured 2 cm beyond the bifurcations.

the model we made the following exceptions: The two coronary arteries, the intercostal arteries, the arteries branching from the celiac axis, and various branches from the subclavian, brachial, and carotid vessels are left out. Arteries present on both sides of the body are modeled identically. These include the renal, carotid, subclavian, brachial, iliac, and the femoral arteries. The coronary arteries are not included because the inflow into the aorta from the aortic valve is measured in the ascending aorta past the coronary bifurcation. However, the coronary arteries take approximately 4%–5% of the cardiac output and hence they should be included if the inflow into aorta is measured immediately after the aortic valve.

The intercostal arteries take less than 1% of the cardiac output and, hence, their neglect does not alter the computed flows significantly. The remaining arteries not included in the model are beyond the initial branching from the aorta, e.g., the branches from the celiac axis. We have no measurements in these arteries and including them would increase the computational time significantly. Finally, left and right arteries are modeled as identical since we only measured the geometry in one side.

The small arteries are modeled as binary asymmetric structured trees attached at the terminals of the large arteries (see Fig. 2). Each of the vessels within the structured trees is modeled as a straight segment of compliant vessel.<sup>20,21</sup> Unlike the large arteries, the structured trees do not mimic the actual geometry of the vessels, but are based on general statistical relationships which are estimated from literature data.<sup>5,14</sup>

## LARGE ARTERIES

Predicting blood flow and pressure in compliant vessels requires three equations. Two equations ensure conservation of volume and momentum, and an equation of state relates the fluid influence on the vessel wall to its compliant properties.

A typical vessel is modeled as an axisymmetric compliant cylinder. The velocity of the fluid enclosed within the cylinder is denoted by  $\mathbf{u}=[u_r(r,x,t),u_x(r,x,t)]$ , where  $r$  is the radial coordinate,  $x$  is the position along the vessel,  $t$  is time,  $u_r$  is the radial velocity, and  $u_x$  is the axial velocity. The blood vessel wall is assumed to be impermeable. Hence, the no-slip condition is satisfied if the velocity of fluid at the wall equals the velocity of the wall. The density  $\rho$  and the viscosity  $\mu$  are taken to be constant. Let  $p(x,t)$  represent the pressure of the fluid and let  $p_0$  (which is constant) represent the diastolic pressure. We assume that the pressure does not vary much over the cross-sectional area of the vessel, i.e.,  $p$  is approximately independent of  $r$ . Let  $R(x,t)$  be the radius of the vessel and let  $A(x,t)=\pi R^2(x,t)$  be the corresponding cross-sectional area. The vessel is assumed to taper exponentially, i.e., the equilibrium radius is  $r_0(x)=r_t \exp(\log(r_b/r_t)x/L)$  when  $p(x,t)=p_0$ . Here,  $r_t$  and  $r_b$  denote the inlet (top) and outlet (bottom) radii of the vessel, and  $L$  denotes the vessel length. Finally, it is assumed that the wall of the vessel undergoes radial motions only, i.e., that the vessel wall is longitudinally tethered.

### Fluid Dynamic Equations for the Large Arteries

*Continuity Equation.* For axisymmetric flow, the continuity equation requires that the divergence of the velocity field vanish, yielding<sup>7</sup>

$$\frac{\partial u_x}{\partial x} + \frac{1}{r} \frac{\partial (ru_r)}{\partial r} = 0. \quad (1)$$

Integrating (1) over the cross-sectional area of the vessel gives

$$\begin{aligned} 0 &= 2\pi \int_0^R \left( \frac{\partial u_x}{\partial x} + \frac{1}{r} \frac{\partial (ru_r)}{\partial r} \right) r dr \\ &= 2\pi \frac{\partial}{\partial x} \int_0^R u_x r dr - 2\pi \frac{\partial R}{\partial x} [ru_x]_R + 2\pi [ru_r]_R. \end{aligned} \quad (2)$$

Since the vessel is longitudinally tethered (i.e., undergoes radial motion only) and the fluid sticks to the vessel wall (due to the no-slip condition)

$$[u_x]_R = 0 \quad \text{and} \quad [u_r]_R = \frac{\partial R}{\partial t}. \quad (3)$$

Moreover, since the cross-sectional area  $A = \pi R^2$ ,

$$2\pi [ru_r]_R = 2\pi R \frac{\partial R}{\partial t} = \frac{\partial A}{\partial t}. \quad (4)$$

Let us define

$$q = 2\pi \int_0^R u_x r dr \quad (5)$$

as the flow (volume/time) through the vessel. Then, the one-dimensional continuity equation can be obtained using (3)–(5) in (2):

$$\frac{\partial q}{\partial x} + \frac{\partial A}{\partial t} = 0. \quad (6)$$

*Momentum Equation.* For axisymmetric flow with no swirl the  $x$ -momentum equation reads<sup>7</sup>

$$\frac{\partial u_x}{\partial t} + u_x \frac{\partial u_x}{\partial x} + u_r \frac{\partial u_x}{\partial r} + \frac{1}{\rho} \frac{\partial p}{\partial x} = \frac{\nu}{r} \frac{\partial}{\partial r} \left( r \frac{\partial u_x}{\partial r} \right). \quad (7)$$

The first three terms represent the axial acceleration of the fluid, and the remaining terms represent the sum of all forces acting on the fluid. In this model the forces are composed of pressure and viscous contributions ( $\nu = \mu/\rho$  is the kinematic viscosity). Generally, the previous equation contains an additional viscous term acting in the longitudinal direction ( $\nu \partial^2 u_x / \partial x^2$ ). In this derivation we have neglected the longitudinal viscous term since it is small compared to the radial term [the right-

hand side of (7)]. The longitudinal viscous term is small because blood vessels are very long in comparison to their radii.

As in the case of the continuity equation a one-dimensional model is obtained by integrating over the cross-sectional area, keeping in mind that  $p$  is assumed constant over that area

$$2\pi \int_0^R \frac{\partial u_x}{\partial t} r dr + 2\pi \int_0^R \left( u_x \frac{\partial u_x}{\partial x} + u_r \frac{\partial u_x}{\partial r} \right) r dr + \frac{A}{\rho} \frac{\partial p}{\partial x} = 2\pi \nu \left[ r \frac{\partial u_x}{\partial r} \right]_R. \quad (8)$$

Using Eqs. (3) and (5) the first term in (8) can be written as

$$2\pi \int_0^R \frac{\partial u_x}{\partial t} r dr = \frac{\partial}{\partial t} \left( 2\pi \int_0^R u_x r dr \right) - \frac{\partial R}{\partial t} 2\pi [ru_x]_R = \frac{\partial q}{\partial t}.$$

Through integration by parts, the continuity Eq. (1) and the relationships in (3) can be used to simplify the second term of (8):

$$\begin{aligned} & 2\pi \int_0^R \left( u_x \frac{\partial u_x}{\partial x} + u_r \frac{\partial u_x}{\partial r} \right) r dr \\ &= 2\pi \int_0^R \left( ru_x \frac{\partial u_x}{\partial x} - u_x \frac{\partial (ru_r)}{\partial r} \right) dr \\ &= 2\pi \int_0^R \frac{\partial u_x^2}{\partial x} r dr = \frac{\partial}{\partial x} \left( 2\pi \int_0^R u_x^2 r dr \right). \end{aligned}$$

Combining the earlier terms with the remaining terms in (8) gives

$$\frac{\partial q}{\partial t} + \frac{\partial}{\partial x} \left( 2\pi \int_0^R u_x^2 r dr \right) + \frac{A}{\rho} \frac{\partial p}{\partial x} = 2\pi \nu \left[ r \frac{\partial u_x}{\partial r} \right]_R. \quad (9)$$

So far we have not made any assumptions about the form of the velocity profile. For pulsatile laminar flow in slightly tapered vessels, the velocity profile is rather flat except for a thin boundary layer of width  $\delta \ll R$ , in which the transition to zero velocity at the wall is made (the no-slip condition).<sup>19,23</sup> Based on these considerations we suggest the following model for the velocity profile

$$u_x = \begin{cases} \bar{u}_x & \text{for } r \leq R - \delta \\ \bar{u}_x (R - r) / \delta & \text{for } R - \delta < r \leq R. \end{cases} \quad (10)$$

Here  $\bar{u}_x(x, t)$  is the axial velocity outside of the boundary layer. According to Lighthill<sup>17</sup> the boundary layer thickness  $\delta$  (for the large arteries) can be estimated from  $(\nu/\omega)^{1/2} = (\nu T/(2\pi))^{1/2} \approx 0.1$  cm, where the kinematic viscosity  $\nu = 0.046$  cm<sup>2</sup>/s,  $\omega$  is the angular frequency, and the period of the cardiac cycle  $T = 1.1$  s. The integrals in (9) can be expressed as power series in  $\delta$ :

$$q = 2\pi \int_0^R u_x r dr = A \bar{u}_x \left( 1 - \frac{\delta}{R} + \mathcal{O}(\delta^2) \right)$$

and

$$2\pi \int_0^R u_x^2 r dr = A \bar{u}_x^2 \left( 1 - \frac{4}{3} \frac{\delta}{R} + \mathcal{O}(\delta^2) \right).$$

Combining these two terms, gives

$$2\pi \int_0^R u_x^2 r dr = \frac{q^2}{A} \left( 1 + \frac{2}{3} \frac{\delta}{R} + \mathcal{O}(\delta^2) \right).$$

The viscous drag force can be evaluated using the velocity profile in (10):

$$2\pi \nu \left[ r \frac{\partial u_x}{\partial r} \right]_R = -\frac{2\pi \nu R \bar{u}_x}{\delta} = -\frac{2\pi \nu R}{\delta} \frac{q}{A} (1 + \mathcal{O}(\delta)). \quad (11)$$

Keeping the leading terms in each component and inserting them into (9) yields the one-dimensional equation

$$\frac{\partial q}{\partial t} + \frac{\partial}{\partial x} \left( \frac{q^2}{A} \right) + \frac{A}{\rho} \frac{\partial p}{\partial x} = -\frac{2\pi \nu R}{\delta} \frac{q}{A}. \quad (12)$$

In the above derivation we assumed that the viscous stress (by the fluid on the wall) is perfectly in phase with the mean velocity. Young and Tsai among others<sup>28,33</sup> defined the viscous stress as a combination of two terms, one accounting for the part in phase with the mean velocity and a second term which is proportional to the time derivative of the velocity. Their derivation is based on oscillatory flow in a rigid vessel where the unsteady term is included. In a rigid vessel  $\bar{u}_x$  can be found in terms of Bessel functions with complex arguments depending on the frequency of the oscillatory flow. The result can be expanded in the limit of either small or large frequencies. In the low frequency limit Poiseuille flow is recovered and at high frequencies the equivalent to (11) is obtained. The solution by Young and Tsai<sup>33</sup> is equivalent to what we have obtained for the small arteries where the viscous effects are more significant (see

section on Small Arteries). For the large arteries the viscous effects are small, and hence, we have not included the unsteady term in the earlier equation. However, such a term can easily be included by changing the coefficient of  $\partial q/\partial t$  in the momentum Eq. (12).

The continuity (6) and momentum (12) equations cannot be solved analytically so a numerical method is called for. In this work, the equations are solved using the two-step Lax–Wendroff method, which requires the equations to be written in conservation form. A conservation form can be obtained by introducing the quantity  $B$  defined below. Note that the cross-sectional area  $A$  is regarded as a function of pressure

$$B(r_0(x), p(x, t)) = \frac{1}{\rho} \int_{p_0}^{p(x, t)} A[r_0(x), p'] dp' \Rightarrow$$

$$\frac{\partial B}{\partial x} = \frac{A}{\rho} \frac{\partial p}{\partial x} + \frac{\partial B}{\partial r_0} \frac{dr_0}{dx}.$$

The last term can be evaluated explicitly and may, therefore, be added to both sides of the momentum Eq. (12). As a result the conservation form is obtained

$$\frac{\partial q}{\partial t} + \frac{\partial}{\partial x} \left( \frac{q^2}{A} + B \right) = - \frac{2\pi\nu q R}{\delta A} + \frac{\partial B}{\partial r_0} \frac{dr_0}{dx}. \quad (13)$$

Equations (6) and (13) constitute our basic one-dimensional model for propagation of blood flow and pressure. However, there are two equations for three dependent variables,  $p$ ,  $q$ , and  $A$ . Therefore, a third relationship (a state equation) is needed.

*State Equation.* The aorta and the large arteries contain smooth muscle, elastin, and collagen. The presence of elastin makes the large arteries capable of considerable expansion and recoil (distensibility). The distensibility of the vessels enables them to store pressure energy as their walls are stretched (during systole) and release it as kinetic energy of flow when the walls are relaxed (during diastole). The storage and release of energy helps to propel the blood toward the tissues during the diastolic phase of the cardiac cycle and promotes a more even flow into the arterioles. The arterioles have a smaller amount of elastin fibers but more smooth muscle fibers, which enables them to regulate the flow by constriction or dilation of their lumen, e.g., during exercise. However, we assume that the subjects studied are at rest and, hence, only the mechanisms of stretch and recoil via the elastin fibers are considered. The distensibility of the large arteries is not purely elastic but the vessels exhibit a viscoelastic behavior.<sup>6</sup> However, in order to keep the model simple, viscoelasticity is disregarded and a simple

relationship is derived from the linear theory of elasticity. Using a purely elastic model is reasonable because viscoelastic effects are small within the physiological ranges of pressure.<sup>29</sup> Assume that the vessels are circular, that the walls are thin ( $h/r_0 \ll 1$ ,  $h$  being the wall thickness), that the loading and deformation are axisymmetric, and that the vessels are tethered in the longitudinal direction. Hence, the external forces can be reduced to stresses acting in the circumferential direction<sup>2</sup> and from what is known as Laplace's law the circumferential tensile stress can be found in the form

$$\tau = \frac{r(p - p_0)}{h} = \frac{E}{(1 - \sigma_x \sigma_\theta)} \frac{(r - r_0)}{r_0},$$

where  $(r - r_0)/r_0$  is the corresponding circumferential strain,  $E$  is Young's modulus in the circumferential direction,  $\sigma_\theta = \sigma_x = 0.5$  are the Poisson ratios in the circumferential and longitudinal directions. Solving for  $p(x, t) - p_0$  give

$$p(x, t) - p_0 = \frac{4}{3} \frac{Eh}{r_0} \left( 1 - \sqrt{\frac{A_0}{A}} \right), \quad (14)$$

where  $A_0 = \pi r_0^2$  is the cross-sectional area when  $p = p_0$ .

The theory that we have just outlined has the property that  $\partial p/\partial A$  decreases with increasing  $p$  (or  $A$ ), contrary to the behavior of real blood vessels, in which  $E$  is not constant but increases as the arterial wall is stretched. This will be addressed in future work. Here, however, we assume that  $E$  is constant (strain independent) at any given location in the arterial tree. We do, however, allow the Young's modulus  $E$  to vary from one location to another. This reflects changes in the elastin content of the vessel wall at different levels of the arterial tree. Specifically, small arteries are stiffer, and we model this by making the Young's modulus  $E$  be a function of the diastolic vessel radius  $r_0$  according to the following formula based on compliance estimates<sup>27,28,31</sup>

$$\frac{Eh}{r_0} = k_1 \exp(k_2 r_0) + k_3. \quad (15)$$

Here  $k_1 = 2.00 \times 10^7$  g/(s<sup>2</sup> cm),  $k_2 = -22.53$  cm<sup>-1</sup>, and  $k_3 = 8.65 \times 10^5$  g/(s<sup>2</sup> cm) are constants.<sup>21</sup>

#### Boundary Conditions for the Large Arteries

The model derived in the previous section predicts blood flow and pressure for a single vessel segment. In order to extend the model to the arterial tree it is necessary to establish relevant boundary conditions.

The system of equations is hyperbolic with a positive wave-propagation velocity much larger than the velocity of the blood. Consequently, three types of boundary con-

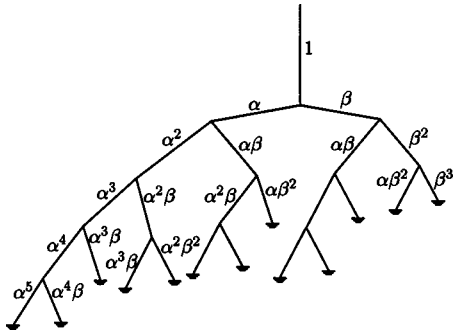


**FIGURE 2.** The structured tree (adapted from Olufsen) (see Ref. 21). At each bifurcation the radii of the daughter vessels are scaled by factors  $\alpha$  and  $\beta$ . Because of the structure in the scaling, some of the subtrees scale with the same factor and for these, the impedance should only be computed once. For example, the impedance of the subtree (scaled by  $\alpha\beta$ ) branching off to the left of the branch scaled by  $\beta$  has already been computed in the subtree branching off to the right of the branch scaled by  $\alpha$ .

ditions must be established: (a) An equation at the inlet to the arterial tree (i.e., at the aortic valve); (b) an equation at the outflow from each of the terminal vessels of the arterial tree (where the small arteries are attached through structured trees, see Figs. 1 and 2); and (c) three equations at each of the bifurcations, since three vessels (a parent and two daughter vessels) meet at each such junction. Each of these boundary conditions should be specified by an equation for either flow, pressure, or a combination of both.

*Inflow Boundary Condition.* At the inlet to the arterial tree the flow is specified using a magnetic resonance measurement of the flow in the ascending aorta (see Fig. 3).

*Bifurcation Conditions.* Assuming that all bifurcations occur at a point and that there is no leakage at the bifurcations, the outflow from any parent vessel ( $pa$ ) must be balanced by the inflow into the daughter vessels ( $d_1$  and  $d_2$ ):

$$q_{pa} = q_{d_1} + q_{d_2}. \quad (16)$$

Vortices can be created at the inlet of the daughter vessels resulting in some loss of energy. In general the loss of energy at bifurcations is minor.<sup>12</sup> Such a loss is customarily expressed in terms of a loss coefficient  $K$  which appears on the right hand side of the Bernoulli equation

$$p_{d_i} = p_{pa} + \frac{\rho}{2} ((\bar{u}_x)_{pa}^2 - (\bar{u}_x)_{d_i}^2) - \frac{K_{d_i} \rho}{2} (\bar{u}_x)_{pa}^2, \quad \text{for } i=1,2. \quad (17)$$

In a one-dimensional model the loss coefficients cannot be estimated analytically, but they can be found either by three-dimensional computations or by physical experiments. In addition, the Bernoulli equation is derived for steady flow in a rigid pipe and hence it does not strictly apply for pulsatile flow in elastic vessels. Previous studies<sup>1,17,28</sup> show that a good approximation which does account for some loss of energy is assuming pressure continuity, i.e., that

$$p_{pa} = p_{d_1} = p_{d_2}. \quad (18)$$

In the simulations presented in this paper Eq. (18) is used at all bifurcations except for the bifurcation from ascending aorta into the aortic arch. At this bifurcation we used (17) with loss coefficients  $K_5=0.75$  and  $K_2=0$ ; the numbers in the subscripts refer to the vessels shown in Fig. 1. These coefficients are estimated based on studies of flow around a bend of a rigid pipe<sup>12</sup> and adjusted to compare with the measured flows. This bifurcation is special because the velocity is maximal before this first major bifurcation which in addition makes a 90° turn. This gives rise to more pronounced vortices and, hence, a larger loss of energy.

*Outflow Boundary Conditions.* The small arteries comprise a collection of binary and asymmetrically structured trees (see Fig. 2). Each such tree has a variable number of generations before the arteriolar level is reached, since that level is defined by a particular vessel radius, and it takes a variable number of generations in an asymmetrically branching tree to reach a specified radius. In the small arteries that connect the large arteries to the arterioles, viscous effects are more important than in the large arteries, and inertial effects are correspondingly less important. Accordingly, we drop the nonlinear terms, but model the viscous effects in greater detail. Another simplification is that we treat each vessel as straight. Together, these assumptions allow for an impedance-based analysis, similar to what would be used for a tree of electrical cables. In particular, we are able to compute the root impedance of each tree of small arteries by a recursive numerical procedure. These root impedances then provide the outflow boundary conditions for the large arteries. This is the subject of the next section.

## SMALL ARTERIES

In order to construct the structured trees located at the terminals of the large arteries (see Figs. 1 and 2), the characteristics of the small vessels must be modeled. Relevant parameters are radius, a bifurcation relationship, asymmetry and area ratios, length, and compliance.

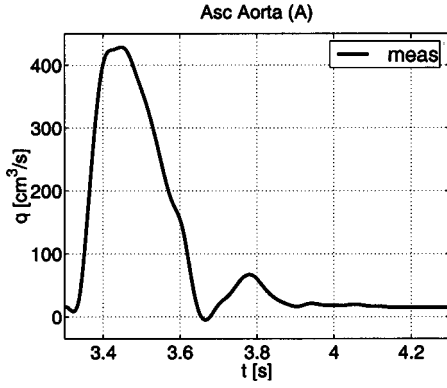


FIGURE 3. The inflow as a function of time. The inflow is a periodic repetition of data measured in the ascending aorta (at A in Fig. 1) during one period lasting 1.1 s.

The structured tree is constructed such that it is geometrically self-similar. All parameters can be specified in terms of the vessel radius. A power law determines how the radius changes across bifurcations

$$(r_0)_{pa}^\xi = (r_0)_{d_1}^\xi + (r_0)_{d_2}^\xi. \quad (19)$$

As in (16), the subscript pa refers to the parent vessel, and the subscripts  $d_1$  and  $d_2$  refer to the two daughter vessels. The power-law has been derived by Murray, Zamir, and Uylings among others<sup>18,30</sup> based on principle of minimum work in the arterial system. The relationship is valid for a range of flows;  $\xi=3.0$  is optimal for laminar flow and  $\xi=2.33$  for turbulent flow. In arterial blood flow a good choice<sup>26</sup> for the exponent is  $\xi=2.76$ .

Combined with equations determining the area and asymmetry ratios, the power law can be used to determine linear scaling ratios between the radii of the daughter vessels and the radius of the parent vessel

$$(r_0)_{d_1} = \alpha(r_0)_{pa}, \quad (r_0)_{d_2} = \beta(r_0)_{pa}$$

and

$$(r_0)_{k,n} = \alpha^k \beta^{n-k} r_0. \quad (20)$$

In these equations  $\alpha$  and  $\beta$  are constants that characterize the asymmetry of the tree (see Fig. 2). Their values will be determined later. The generation number is denoted by  $n$ , with  $n=0$  corresponding to the vessel that forms the root of the tree. The constant  $r_0$ , with no further subscript, refers to the radius of the root vessel. There may be as many as  $2^n$  vessels in the  $n$ th generation; however, because some branches may already have terminated, this number will often be smaller. In addition, there are at most  $n+1$  different size branches in generation  $n$ , corresponding to  $k$  choices of the scaling

factor  $\alpha$ , and  $n-k$  choices of the scaling factor  $\beta$ , where  $0 \leq k \leq n$ .

The structured tree continues to branch until the radius of any vessel is smaller than some given minimum value ( $r_{min}$ ). The arterioles are muscular vessels which are able to dilate and contract severalfold regulating the supply of blood to the tissue. Assume that the subject studied is at rest. Then, the minimum radius can be selected such that the resistances of the structured trees correspond to the resistances of the vascular beds.

The asymmetry of the vessels can be characterized from the area ( $\eta$ ) and asymmetry ( $\gamma$ ) ratios,<sup>34</sup> which can be defined by

$$\eta = \frac{(r_0)_{d_1}^2 + (r_0)_{d_2}^2}{(r_0)_{pa}^2} \quad \text{and} \quad \gamma = \left( \frac{(r_0)_{d_2}}{(r_0)_{d_1}} \right)^2.$$

The parameters  $\xi$ ,  $\eta$ , and  $\gamma$  are not independent but are related by

$$\eta = \frac{1 + \gamma}{(1 + \gamma^{\xi/2})^{2/\xi}}. \quad (21)$$

Consequently, if the area-ratio  $\eta$  and the exponent  $\xi$  are known, the asymmetry-ratio  $\gamma$  can be calculated. Using an area ratio of  $\eta=1.16$  and the power  $\xi=2.76$ , the asymmetry-ratio  $\gamma=0.41$ . The area-ratio  $\eta$  and the exponent  $\xi$  have been estimated based on studies by Papa-georgiou *et al.*<sup>22</sup> and Uylings<sup>30</sup> The scaling parameters  $\alpha$  and  $\beta$  can be found from  $\xi$  and  $\gamma$ :

$$\alpha = (1 + \gamma^{\xi/2})^{-1/\xi} = 0.9 \quad \text{and} \quad \beta = \alpha \sqrt{\gamma} = 0.6. \quad (22)$$

The length of each vessel can be related to the radius using a constant length-to-radius ratio. Based on studies by Iberall<sup>11</sup> we have chosen the length-to-radius ratio  $l_{\pi} = L/r_0 \approx 50$ . Iberall estimated this length-to-radius ratio based on branches from the small arteries such as the renals, the femoral arteries, the mesenteric arteries, and the cerebral artery.

In order to compute the compliance of the small arteries, information on how the wall-thickness  $h$  and Young's modulus  $E$  change or depend on other parameters throughout the tree is needed. Such a relationship has been estimated for the large arteries and the small arteries are essentially composed of the same types of tissue, hence, (15) has been taken to apply for the small arteries and arterioles.

As in the case of the large arteries, equations for blood flow and pressure in the small arteries can be derived from the axisymmetric Navier–Stokes equations. However, while inertia effects are more important in the

large systemic arteries, viscous effects become more important in the small arteries.<sup>6</sup> Hence, we neglect the nonlinear inertial terms. This approach is based on the work originally discussed by Womersley, but later refined by Pedley and Atabek and Lew.<sup>2,20,24,32</sup> Assuming that the flow and pressure are periodic, the momentum Eq. (7) can be written as a Bessel equation, which can be solved analytically. This analytical solution provides a frequency-dependent relationship between flow and pressure in the form of an impedance condition.

#### Fluid Dynamic Equations for the Small Arteries

Linearizing the momentum Eq. (7) yields

$$\frac{\partial u_x}{\partial t} + \frac{1}{\rho} \frac{\partial p}{\partial x} = \frac{\nu}{r} \frac{\partial}{\partial r} \left( r \frac{\partial u_x}{\partial r} \right). \quad (23)$$

Assuming that all variables are periodic they can be written in the form  $u_x(r, x, t) = U_x(r, x)e^{i\omega t}$ ,  $p = P(x)e^{i\omega t}$ . Hence, (23) can be written as

$$i\omega U_x + \frac{1}{\rho} \frac{\partial P}{\partial x} = \frac{\nu}{r} \frac{\partial}{\partial r} \left( r \frac{\partial U_x}{\partial r} \right). \quad (24)$$

Since the small vessels do not taper, the solution to (24) is given by

$$U_x = \frac{1}{i\omega\rho} \frac{\partial P}{\partial x} \left( 1 - \frac{J_0(rw_0/r_0)}{J_0(w_0)} \right), \quad (25)$$

where  $w_0^2 = i^3 w^2$  ( $w^2 = r_0^2 \omega / \nu$  is the Womersley number) and  $J_0(x)$  and  $J_1(x)$  are the zeroth and first order Bessel functions. Similar to the large arteries the flow-rate  $q = Qe^{i\omega t}$  is given by

$$Q = 2\pi \int_0^{r_0} U_x r dr \Leftrightarrow i\omega Q = \frac{-A_0}{\rho} \frac{\partial P}{\partial x} (1 - F_J), \quad (26)$$

where

$$F_J = \frac{2J_1(w_0)}{w_0 J_0(w_0)}. \quad (27)$$

The viscous stress  $\tau_{rx} = \mathcal{T}e^{i\omega t}$  by the wall on the fluid can be determined from the solution to the linearized Navier–Stokes Eq. (23):

$$\mathcal{T} = \mu \left. \frac{\partial U_x}{\partial r} \right|_{r=r_0} = \frac{\mu}{A_0 r_0} \frac{w_0^2 F_J}{2(1 - F_J)} Q. \quad (28)$$

Expanding (28) for small values of  $w_0$  yields

$$\begin{aligned} \mathcal{T} &= \frac{\mu}{A_0 r_0} \left[ -4 + \frac{w_0^2}{6} + \mathcal{O}(w_0^4) \right] Q \Leftrightarrow \\ \tau_{rx} &= -\frac{4\mu}{A_0 r_0} \left[ 1 + \frac{r_0^2}{24\nu} \frac{d}{dt} + \mathcal{O}(\omega^2) \right] q. \end{aligned} \quad (29)$$

The first term of (29) is similar to the viscous stress (11) obtained from the simple boundary-layer consideration in (10) except that the above term corresponds to a parabolic velocity profile. The second term corresponds to the unsteady term obtained by Young and Tsai.<sup>33</sup> However, they modified the coefficients based on empirical data.

The one-dimensional continuity equation for the small arteries is the same as the one for the large arteries. Using the state Eq. (14) the continuity (6) can be written as

$$C \frac{\partial p}{\partial t} + \frac{\partial q}{\partial x} = 0, \quad C = \frac{\partial A}{\partial p},$$

where  $C$  is the compliance. The compliance can be approximated by linearizing the state Eq. (14):

$$C = \frac{\partial A}{\partial p} = \frac{3A_0 r_0}{2Eh} \left( 1 - \frac{3pr_0}{4Eh} \right)^{-3} \approx \frac{3A_0 r_0}{2Eh}, \quad (30)$$

since  $Eh \gg pr_0$ .

Because the inflow into the arterial tree is periodic the flow and pressure will be periodic, and hence they can be expressed using complex periodic Fourier series of the form

$$\phi(x, t) = \sum_{k=-\infty}^{\infty} \Phi(x, \omega_k) e^{i\omega_k t},$$

$$\Phi(x, \omega_k) = \frac{1}{T} \int_{-T/2}^{T/2} \phi(x, t) e^{-i\omega_k t} dt,$$

where  $\omega_k = 2\pi k/T$ . The Fourier series should be used for  $\phi = p(x, t), q(x, t), z(x, t)$  or in the frequency domain  $\Phi = P(x, \omega), Q(x, \omega), Z(x, \omega)$ . Using the Fourier series and the compliance approximation in (30) the continuity equation can be transformed as

$$i\omega C P + \frac{\partial Q}{\partial x} = 0. \quad (31)$$

The momentum (26) and continuity (31) equations determine the flow resulting from an oscillatory pressure

gradient in a straight vessel where the amplitude and phase depend on the compliance of the wall and the viscosity of the blood. The equations are periodic with period  $T$  and apply to any vessel of length  $L$ . Differentiating (31) with respect to  $x$  and inserting the result in (26) gives a reduced wave equation of the form

$$\frac{\omega^2}{c^2}Q + \frac{\partial^2 Q}{\partial x^2} = 0 \quad \text{or} \quad \frac{\omega^2}{c^2}P + \frac{\partial^2 P}{\partial x^2} = 0 \quad (32)$$

with the wave-propagation velocity

$$c = \sqrt{\frac{A_0(1-F_J)}{\rho C}}. \quad (33)$$

Solving (31) and (32) yields

$$Q(x, \omega) = a \cos(\omega x/c) + b \sin(\omega x/c),$$

$$P(x, \omega) = i \sqrt{\frac{\rho}{CA_0(1-F_J)}} (-a \sin(\omega x/c) + b \cos(\omega x/c)),$$

where  $a$  and  $b$  are arbitrary constants of integration.

Using the terminology from electrical cables, with  $P$  playing the role of voltage and  $Q$  playing the role of current, the impedance  $Z(x, \omega)$  can be related to pressure and flow by

$$Z(x, \omega) = \frac{P(x, \omega)}{Q(x, \omega)} = \frac{ig^{-1}(b \cos(\omega x/c) - a \sin(\omega x/c))}{a \cos(\omega x/c) + b \sin(\omega x/c)},$$

where  $g = cC = \sqrt{CA_0(1-F_J)/\rho}$ . At  $x=L$

$$Z(L, \omega) = \frac{ig^{-1}(b \cos(\omega L/c) - a \sin(\omega L/c))}{a \cos(\omega L/c) + b \sin(\omega L/c)}$$

and at  $x=0$ :

$$Z(0, \omega) = \frac{ib}{ga}, \quad (34)$$

where

$$\frac{b}{a} = \frac{\sin(\omega L/c) - igZ(L, \omega)\cos(\omega L/c)}{\cos(\omega L/c) + igZ(L, \omega)\sin(\omega L/c)}.$$

Inserting  $b/a$  into (34) gives

$$Z(0, \omega) = \frac{ig^{-1} \sin(\omega L/c) + Z(L, \omega)\cos(\omega L/c)}{\cos(\omega L/c) + igZ(L, \omega)\sin(\omega L/c)}. \quad (35)$$

For any vessel, the input impedance for zero frequency, or in the electrical terminology the direct current (DC) impedance, can be found as

$$Z(0, 0) = \lim_{\omega \rightarrow 0} Z(0, \omega) = \frac{8\mu l_{rr}}{\pi r_0^3} + Z(L, 0), \quad (36)$$

where  $l_{rr} = L/r_0$  is the length-to-radius ratio. Equation (36) suggests that in general (for any network) the root impedance will be proportional to  $r_0^{-3}$ . Since the structured tree is terminated when the radius of any branch is smaller than some given minimum value,  $r_{\min}$ , the constant of proportionality cannot be derived analytically.

#### Boundary Conditions for the Small Arteries

Analogous to the large arteries, Eqs. (26) and (31) predict blood flow and pressure for a single vessel segment. In order to compute the impedance at the root of the structured tree it is necessary to establish relevant boundary conditions. In this case, the relevant boundary conditions are outflow boundary conditions and bifurcation conditions.

*Bifurcation Conditions.* The bifurcation conditions are similar to those established for the large arteries. As in the case of the large arteries we assume that there is no leakage at the bifurcation so that the flow is conserved. Moreover, the pressure is continuous since any pressure difference across a junction, which would arise due to the nonlinear terms, is being neglected. Therefore, the bifurcation is analogous to a transmission-line network where the admittances ( $Y = 1/Z$ ) add

$$\frac{1}{Z_{pa}} = \frac{1}{Z_{d1}} + \frac{1}{Z_{d2}}. \quad (37)$$

*Outflow Boundary Conditions.* Since viscosity is taken into account in the fluid dynamics of the structured tree, it is not necessary to include lumped resistance elements at the leaves of the structured tree, i.e., the terminal resistance of the structured trees can be set to zero. The various parts of the body serve different needs and hence show a variation in the peripheral resistance. Having a zero terminal resistance for the structured trees thus requires that the minimum radii ( $r_{\min}$ ) at the terminals are chosen individually for each of the structured trees. While  $r_{\min}$  may vary among the different structured trees, it is kept constant within each of them.

## THE ROOT IMPEDANCE OF THE SMALL ARTERIES AND COUPLING OF SMALL AND LARGE ARTERIES

As described earlier, all parameters for the structured tree are determined as functions of the vessel radius. Hence,  $g$  and the length  $L$  can be determined as functions of the vessel radius. Furthermore, the geometric self-similarity makes it possible to compute the root impedance  $Z(0, \omega)$  for each of the structured trees shown in Fig. 1. Since the terminal impedance is known (and constant) within each of the structured trees, the impedance at the beginning of all the terminal vessels can be found using (35). Jumping up one generation, the impedance at the end of all parent vessels can be found using (37). Again (35) can be used to find the impedance at the beginning of the vessels at this level. Continuing in this manner the impedance can be found at the root of the structured tree (for details see Algorithms for the Small Arteries in Appendix B). Computing the root impedance using the method described earlier would be very expensive if the structure of the small arteries were not accounted for. As shown in Fig. 2, some subtrees scale with the same factors as subtrees in which the impedance has already been computed. Assuming that all terminal branches are terminated with the same peripheral resistance, subtrees with identical paths will have the same root impedance, and need not be re-evaluated. This structure reduces the computation from order  $\mathcal{O}(2^n)$  to  $\mathcal{O}(n^2)$  where  $n$  is the maximum number of generations of the structured tree.

As stated earlier, a complete binary tree has  $2^n$  branches at the  $n$ th generation. In our case the tree is structured such that the radii of the vessels at the  $n$ th generation are given by (20). For the whole tree with  $n$  generations there would be

$$\sum_{j=0}^n \sum_{k=0}^j 1 = \frac{(n+1)(n+2)}{2} = \mathcal{O}(n^2)$$

different impedances which must be calculated. For the structured tree (see Fig. 2) some branches terminate early and hence the number of impedances that must be calculated is smaller.

By inverse Fourier transform the results for  $Z(x, \omega)$  can then be transformed to obtain  $z(x, t)$ . Using the convolution theorem it is possible to arrive at an analytic relationship between  $p$  and  $q$ :

$$p(x, t) = \int_{t-T}^t q(x, \tau) z(x, t - \tau) d\tau. \quad (38)$$

This new outflow boundary condition for the large arteries should be evaluated for each of the terminals of the

large arteries (see Algorithms for the Small Arteries in Appendix B).

In order to evaluate the above convolution integral (38) for all times during a period, the impedance  $Z(\omega)$  should be determined for all discrete angular frequencies  $\omega_k = 2\pi k/T$ , where  $k = -N/2, \dots, N/2$  and  $N$  is the number of timesteps per period. Assuming that  $z(x, t)$  is real,  $Z$  must be self-adjoint

$$Z(0, \omega_{-k}) = \overline{Z(0, \omega_k)}.$$

Hence, only  $Z(0, \omega_k)$  for  $k = 0, 1, \dots, N/2$  need to be determined.

## RESULTS

Our aim was to show that the structured tree model provides a feasible outflow boundary condition for determining blood flow and pressure in the large arteries. We verified that our model can reproduce the essential characteristics of the arterial pulse both qualitatively and quantitatively by comparing our model with data measured using magnetic resonance techniques.

All simulations in this paper were based on the same set of parameters. Most lengths and diameters were based on magnetic resonance measurements. At locations where measured data were not available, lengths and diameters were estimated from combining literature data with measured and computed flows. All geometric parameters used to specify the large arteries are shown in Table 1. The parameters representing  $Eh/r_0$  were chosen using (15), while density ( $\rho = 1.055 \text{ g/cm}^3$ ) and viscosity ( $\mu = 0.049 \text{ g/(cm s)}$ ) were kept constant. The parameters for the structured trees followed the choices discussed in the section on Small Arteries. The terminal resistances for the small arteries were all set to zero. In order to take the variation in peripheral resistance into account, four different minimum radii  $r_{\min} = 0.01, 0.02, 0.03 \text{ cm}$  were chosen for the structured trees (see Table 1).

The total cross-sectional area of the systemic arteries increases from  $5 \text{ cm}^2$  at the root of the aorta to  $400 \text{ cm}^2$  at the arterioles. The maximum (systolic) pressure of the large arteries increases away from the heart, towards the periphery, while the mean pressure decreases.<sup>6</sup> The increase of systolic pressure is mainly due to tapering and branching of the large arteries and the peripheral resistance in the arterioles. As a result of these features the flow and pressure waves are reflected. In the large arteries, the reflected wave is superimposed on the pressure wave, increasing the systolic pressure. At the same time the large increase in cross-sectional area causes a decrease in mean pressure. Within each of the vessels the same effect can be seen on the flow wave, however, at the bifurcations the flow decreases. These effects were

**TABLE 1. Geometrical data, i.e., length, inlet (top) and outlet (bottom) radii, and the minimum radius for the structured trees. The numbering in the left column refers to the numbers shown in Fig. 1. Data labeled m are measured on the magnetic resonance images and data labeled e are estimated. All the measured radii and lengths have an accuracy of  $\pm 1$  mm. In the computations, the values listed in the table are used (with two decimal points); these values are selected so as to approximately match the measured radius accounting for the exponential tapering defined in Large Arteries.**

No.	Artery	L (cm)	$r_t$ (cm)	$r_b$ (cm)	$r_{\min}$ (cm)	
1	Ascending aorta	m	7.0	1.25	1.14	...
5	Aortic arch	m	1.8	1.14	1.11	...
7	Aortic arch	m	1.0	1.11	1.09	...
9	Thoracic aorta	m	18.8	1.09	0.85	...
11	Abdominal aorta	m	2.0	0.85	0.83	...
13	Abdominal aorta	m	2.0	0.83	0.80	...
15	Abdominal aorta	m	1.0	0.80	0.79	...
17	Abdominal aorta	m	6.0	0.79	0.73	...
19	Abdominal aorta	m	3.0	0.73	0.70	...
20	External iliac	m	6.5	0.45	0.43	...
21	Femoral	m	13.0	0.43	0.40	...
24	Femoral	e	44.0	0.40	0.30	0.01
22	Internal iliac	e	4.5	0.20	0.20	0.01
23	Deep femoral	e	11.0	0.20	0.20	0.01
2	Anonyma	e	3.5	0.70	0.70	...
3, 8	Subcl. and brach.	e	43.0	0.44	0.28	0.01
4	R. com. carotid	e	17.0	0.29	0.28	0.02
6	L. com. carotid	e	19.0	0.29	0.28	0.03
10	Celiac axis	e	3.0	0.33	0.30	0.02
12	Sup. mesenteric	e	5.0	0.33	0.33	0.02
14,16	Renal	e	3.0	0.28	0.25	0.02
18	Inf. mesenteric	e	4.0	0.20	0.18	0.01

also present in our simulations (see Figs. 4–6). Furthermore, the velocity of the reflected wave is slower than the velocity of the main wave. Consequently, the reflected wave separates from the incoming wave and becomes more prominent at peripheral locations than at proximal locations<sup>9,16</sup> (see Fig. 4). Finally, the steepness of the incoming pressure and flow profiles increases towards the periphery. This is due to changes in the wave-propagation which, because of an increased Young's modulus, is larger for the small vessels<sup>4</sup> (see Fig. 5).

The flow data were measured using magnetic resonance techniques in a 32 year old male weighing 65 kg and being 178 cm tall. His average heart rate at rest was 51 beats per minute and his systolic and diastolic blood pressures were 120/80 mmHg (measured with a cuff); for further details see Appendix A. These pressure measurements corresponded well to the pressures computed at the left subclavian artery (see Fig. 8).

The flows shown in Fig. 7 were measured at the locations identified in Fig. 1. The corresponding pressures, computed using our model are shown in Fig. 8.

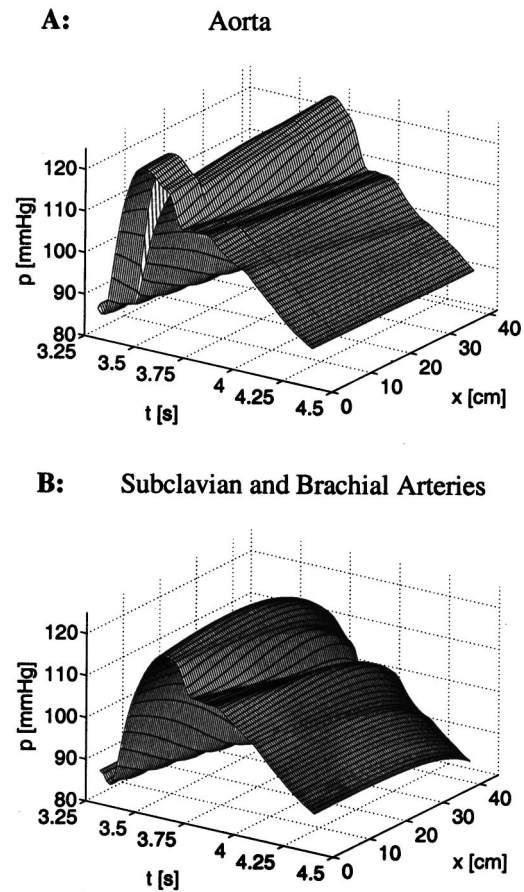


**FIGURE 4.** The graphs show pressure (mmHg) as a function of space  $x$  and time  $t$ . The top graph shows the pressure along the aorta and the bottom graph shows the pressure of the subclavian and brachial arteries. The reason why the aortic pressure has a discrete jump after 7 cm is the loss of energy between the ascending aorta, anonyma, and the aortic arc (vessels 1, 2, and 5 in Fig. 1). The pressure in the subclavian and brachial arteries initially increases and then decreases in order to accommodate the boundary condition arising from the structured tree.

## CONCLUSION

The purpose of this study was to derive the equations and boundary conditions needed for predicting blood flow and pressure in the systemic arteries and to use these in a case study in which the geometry was based on anatomical data and the other model parameters were based on physical laws but adjusted to compare with the measured flow profiles. This was achieved by using a one-dimensional fluid-dynamics model, including the large and small arteries. The geometry of the large arteries was modeled combining measured data for the vessel length, inlet (top) and outlet (bottom) radii with an empirical law modeling the exponential taper of the vessels. The geometry of the small vessels was based on literature data and adjusted such that the peripheral resistance matched the measured flows. For large and

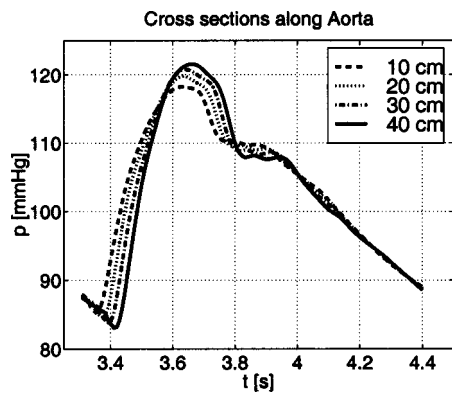


FIGURE 5. The graph shows the aortic pressure at four locations along the aorta. From these profiles it becomes easy to see that the steepness of the wave front is increased at more peripheral locations.

small vessels the flow and pressure were determined using the one-dimensional theory derived from the Navier–Stokes equations. For the large arteries, flow and pressure were determined at all points along the vessels but for the small arteries (the terminals of the large arteries) an impedance relationship (pressure versus flow) constituting a boundary condition for the large arteries was determined.

Figures 4–6 show that the resulting pressure and flow profiles all have the correct characteristics. The systolic pressure increases away from the heart. The mean pressure drops slowly. The steepness of the incoming pressure profile increases towards the periphery. Finally, the wave propagation velocity of the reflected dicotic wave is slower than that of the main wave, and hence, the reflected wave separates from the main wave peripherally. This can be seen in Fig. 4, where the distance between the main pressure wave and smaller reflected (the dicotic) wave is increased towards the periphery. In addition to showing reasonable characteristics, our results reveal that the one-dimensional model provides an

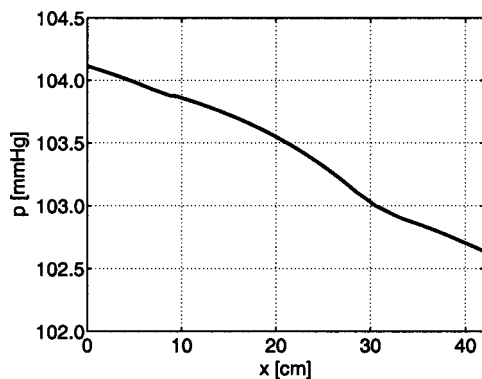


FIGURE 6. The graph shows the decrease of the mean pressure along the aorta.

excellent quantitative agreement with measured data. For a correct quantitative comparison, measurements and computations were carried out in vessels where the geometry and inflow were matched. The reason for this was that the pressure and flow profiles are highly dependent on these factors and vary significantly even among healthy young people.<sup>19</sup>

The advantage of modeling the small arteries by applying structured trees at all terminals of the large arteries is that it gives a physiological boundary condition which is able to include wave-propagation effects. Furthermore, the structured tree model has only two parameters that need to be estimated, the compliance of the vessels and the radii at which the structured trees are terminated. Because we did not apply any impedance at the terminals of the structured tree, the peripheral impedance for the large arteries was obtained entirely from the solution to the linearized equations in the binary asymmetrically structured tree.<sup>21</sup>

As mentioned in Small Arteries, the diameter of the small arteries varies considerably and so does the peripheral resistance of these very small vessels which have a strong muscular wall. This is consistent with the observations<sup>10</sup> that it is the arterioles, and not the capillaries, which generate the peripheral resistance. The total peripheral resistance of the different organs vary, hence, it is important to choose the minimum radius individually for each of the structured trees, i.e., for each of the terminal branches of the large arteries. However, unless the diameters of the small vessels are changed dynamically during the time course of a simulation the model does not reflect dynamics due to auto- or baroreceptor regulation. The simulations in this paper do not incorporate dynamic change of the small vessels and hence reflect that the individual studied is at rest.

In summary, our study has shown the feasibility of limiting the computational domain such that blood flow and pressure can be predicted using a one-dimensional model consisting of large and small arteries. The computational domain is limited because of our use of the structured tree outflow conditions. The structure of the trees representing the smaller vessels allows the complexity of the computations to be decreased from  $\mathcal{O}(2^n)$  to  $\mathcal{O}(n^2)$ , where  $n$  is the number of generations in the structured tree. Furthermore, since the structured trees represent branching vessels, we are able to model the propagation of the wave through the small vessels and thus determine a dynamic impedance characterizing the underlying physiology.<sup>19,21</sup>

One might argue that the structured tree model is too complicated and that the much simpler windkessel model is adequate because it can also provide a dynamic outflow boundary condition. The windkessel model is based on parameters describing the total resistance and compliance.<sup>28</sup> It has been shown that the windkessel

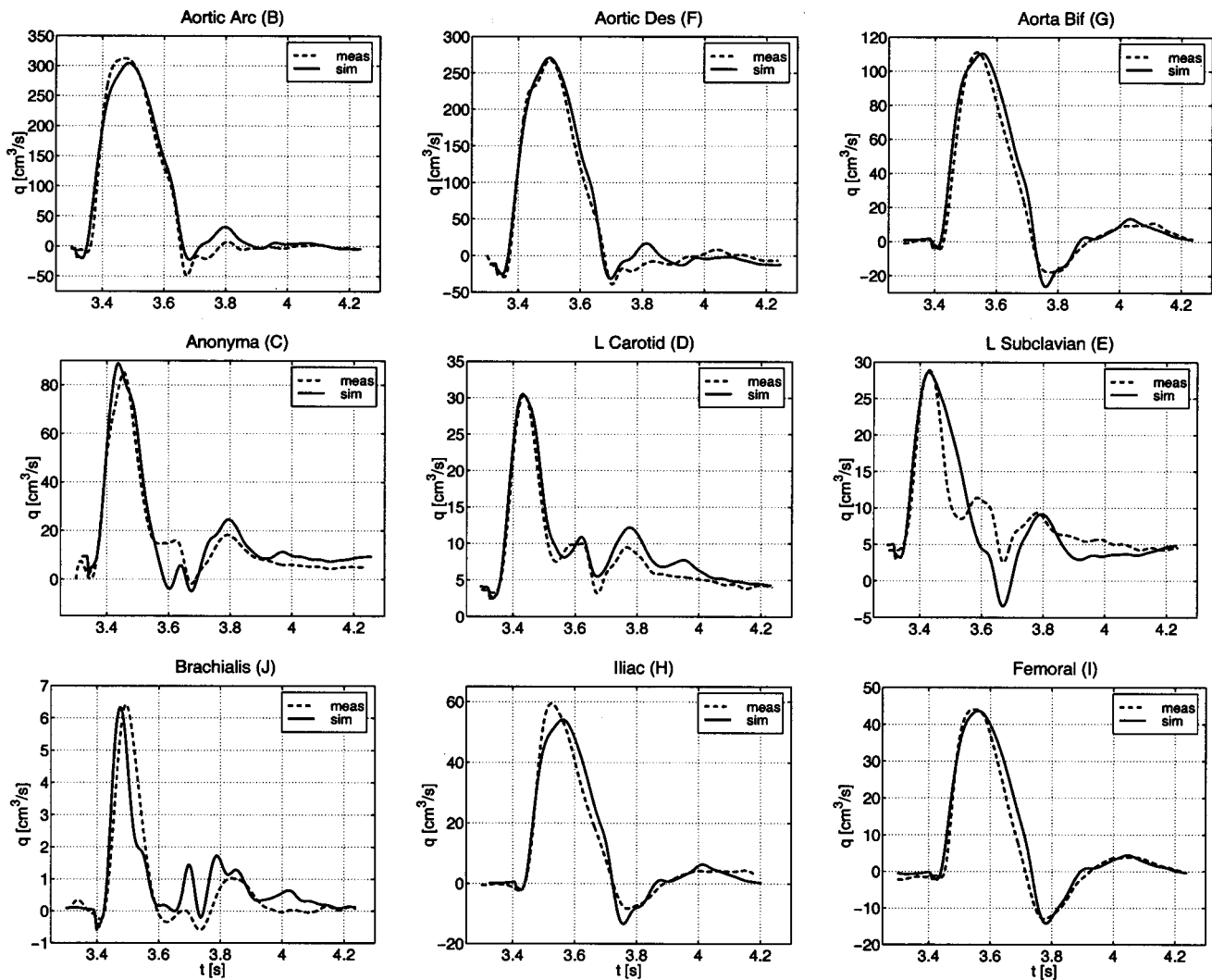


FIGURE 7. Measured and simulated flows. The letter in parenthesis indicates where the flow is measured as shown in Fig. 1. The figure shows the nine flows measured peripherally to the ascending aorta (the inflow into the arterial tree, see Fig. 3).

model cannot capture the dynamics of higher frequencies.<sup>21</sup> Moreover, it is not obvious how the windkessel parameters should be estimated for the large vessels. However, it is possible to relate the parameters of the commonly used windkessel model to our structured tree model, which would enable comparison of the two models. The total resistance of the windkessel model corresponds to the DC impedance of the structured tree, while the peripheral resistance corresponds to the high-frequency limit of the structured tree. Finally, the total compliance of the windkessel model can be related to the slope at which the impedance of the structured tree decreases from zero frequency towards higher frequencies.

Nevertheless, we find that the structured tree model has several important advantages. The structured tree is based on the underlying physiology and it includes wave propagation effects which enable our model to capture the observed oscillations of the impedance in the part of

the arterial system that it models. Second, the structured tree model can predict flow and pressure not only in the large but also in the small arteries, i.e., shifting the purpose of the structured tree from being a boundary condition to being a more active part of the model.

The idea of using a structured tree in which a simpler set of equations is solved could also be applied to other areas involving flow in tree-like structures such as flow and water depth in a river delta. However, the use of the outflow boundary condition presented here is only applicable to phenomena in which there is some scaling law that gives rise to a structured tree.

## APPENDIX A: MAGNETIC RESONANCE IMAGING

Written informed consent was obtained from the subject in accordance with the regional ethical committee on

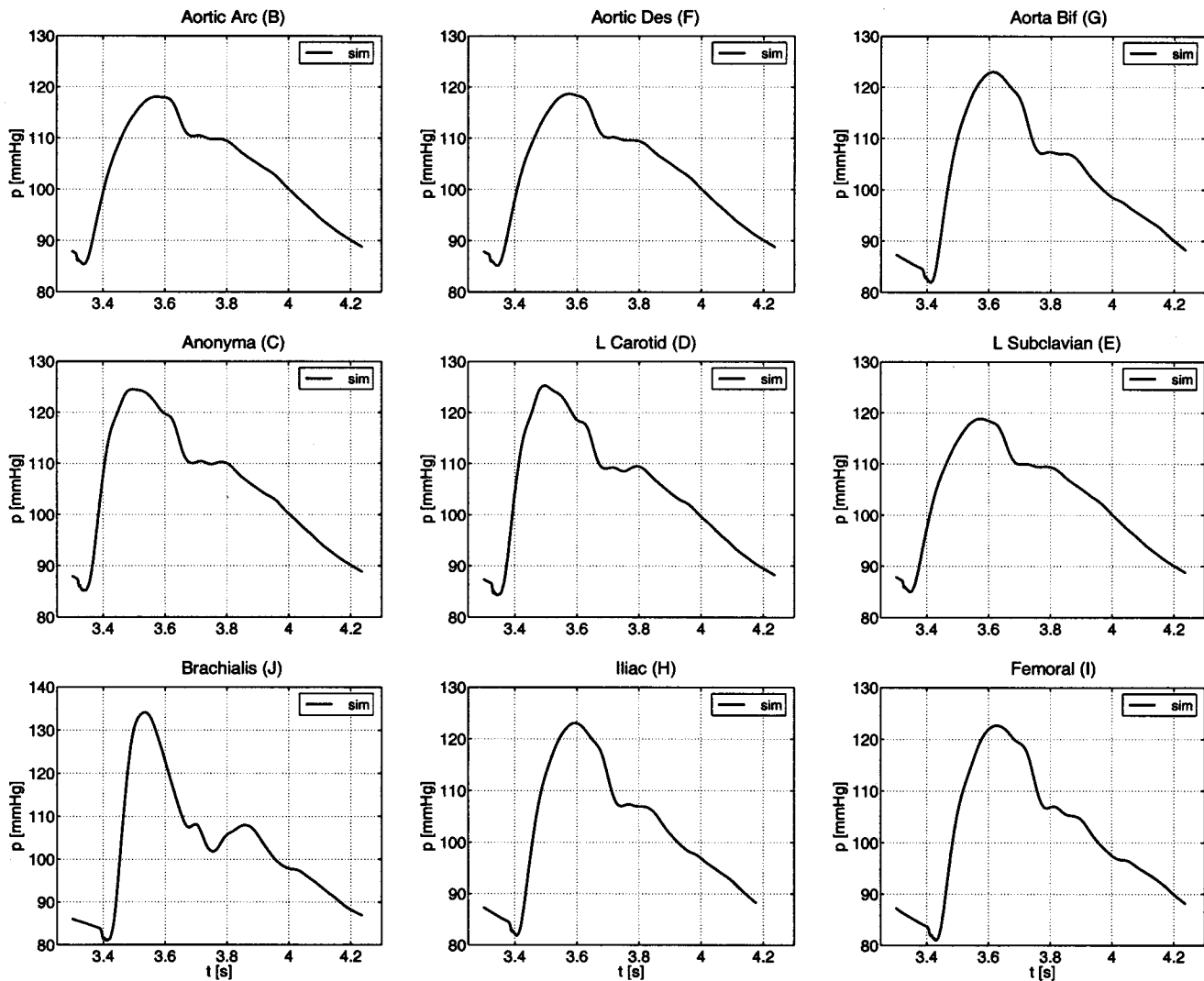


FIGURE 8. Simulated pressures corresponding to the flows shown in Fig. 7.

human research and the Helsinki Declaration. The subject was a 25 years old healthy male subject without any known cardiac disease with a body surface area of 1.94 m<sup>2</sup>. The magnetic resonance imaging (MRI) investigation was performed on a 1.5 T whole body system (Gyrosan ACS-NT 15, Philips Medical Systems, Best, The Netherlands). The subject was examined in the supine position. To minimize motion artifacts caused by heart motion, image acquisition was synchronized to the R wave of the electrocardiogram (ECG). The body coil was used for radio frequency transmission while circular surface coils and a dedicated five-element cardiac synergy coil was used as receiver for the peripheral and greater vessels, respectively. Multistack, multislice gradient-echo scouts were performed at each vessel location to estimate the geometry of the different vessels for the quantitative flow measurements. Based on these scout images, transverse gradient-echo, velocity-encoded images were ac-

quired. The imaging parameters were echo time 6.3 ms, time resolution 30 ms, flip angle 20°, spatial in-plane resolution 1.25×1.25 mm, slice thickness 6 mm, two signal averages, and velocity encoding ±80 cm/s. Total imaging time for a complete measurement series was approximately one hour with an average heart rate of 51 beats per minute.

#### MRI Data Analysis

The volumetric flow rates from the different vessels were calculated as the product of the cross-sectional area and spatial mean velocity in each time frame. The velocity was calculated from the magnetic resonance phase images assuming linearity between magnetic resonance signal phase and velocity. The vessel cross-sectional areas were automatically segmented using active contour model algorithms to define the vessel boundaries.<sup>15</sup> In

addition, velocities above the Nyquist limit of  $\pm 80$  cm/s were manually unwrapped by adding the velocity value corresponding to  $\pm 2\pi$ .

## APPENDIX B: ALGORITHMS

### Discrete Fluid Dynamic Equations for the Large Arteries

For the large vessels it is necessary to compute flow and pressure for each of the vessels, but for the small vessels only the impedances at the terminals of the large vessels (at the outflow) are of interest. For the large vessels the equations are solved using the two-step Lax–Wendroff method and for the small vessels the equations are solved using a recursive approach.

The continuity (6) and momentum (13) equations in conservation form can be solved using the two-step Lax–Wendroff method. Using the state Eq. (14) the pressure terms of the continuity and momentum equations can be expressed as functions of  $A$ . Hence, the continuity and momentum equations can be solved for  $q$  and  $A$ . The flux of (6) and (13) are given by

$$\mathbf{R} = (R_1, R_2) = \left( q, \frac{q^2}{A} + B \right) \quad (\text{B1})$$

and the right-hand side by

$$\mathbf{S} = (S_1, S_2) = \left( 0, -\frac{2\pi\nu q R}{\delta A} + \frac{\partial B}{\partial r_0} \frac{dr_0}{dx} \right). \quad (\text{B2})$$

Using the definitions for  $\mathbf{R}$  and  $\mathbf{S}$ , and assuming that  $\mathbf{U} = (A, q)$  the continuity (6) and momentum (13) equations can be written as

$$\frac{\partial}{\partial t} \mathbf{U} + \frac{\partial}{\partial x} \mathbf{R} = \mathbf{S}.$$

Assume that the grid is uniform with the distance between any two grid-points being given by  $\Delta x$  and  $\Delta t$  for the spatial and temporal axes, respectively (see Fig. B1). Then, the Lax–Wendroff method is stable if the Courant Friedrichs Lewy (CFL) condition<sup>8</sup> is fulfilled for both choices of sign

$$\frac{\Delta t}{\Delta x} \leq \left| \frac{q}{A} \pm c \right|^{-1},$$

where  $q/A \pm c$  is the characteristic wave-propagation velocity,  $q/A$  is the mean velocity and

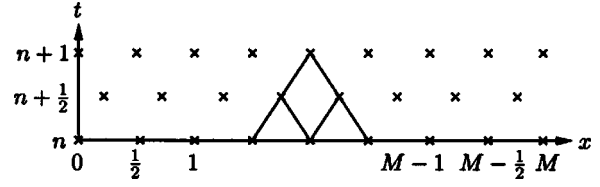


FIGURE B1. The values of  $q$  and  $A$  at  $n+1$  are determined in two steps. During the first step, intermediate values at  $n+1/2$  are determined from values at  $n$ . At the second step the values at  $n+1$  are determined from the intermediate values.

$$c = \sqrt{\frac{A}{\rho} \frac{\partial p}{\partial A}}$$

is the wave speed (for details see Olufsen).<sup>20</sup>

Define  $\mathbf{U}_m^n = \mathbf{U}(m\Delta x, n\Delta t)$  where  $0 < n \leq N$  denotes the current time step (and not generations of the structured trees as in previous sections) and  $0 < m \leq M$  denotes the position along a vessel divided into  $M$  subintervals. Similarly definitions can be made for  $\mathbf{R}$  and  $\mathbf{S}$ . The flow  $q$  and cross-sectional area  $A$  at time-level ( $n+1$ ) can be found from

$$\begin{aligned} \mathbf{U}_m^{n+1} = & \mathbf{U}_m^n - \frac{\Delta t}{\Delta x} (\mathbf{R}_{m+1/2}^{n+1/2} - \mathbf{R}_{m-1/2}^{n+1/2}) \\ & + \frac{\Delta t}{2} (\mathbf{S}_{m+1/2}^{n+1/2} + \mathbf{S}_{m-1/2}^{n+1/2}). \end{aligned} \quad (\text{B3})$$

The intermediate values  $\mathbf{R}_{m+1/2}^{n+1/2}$ ,  $\mathbf{S}_{m+1/2}^{n+1/2}$ ,  $\mathbf{R}_{m-1/2}^{n+1/2}$ , and  $\mathbf{S}_{m-1/2}^{n+1/2}$  at time-level  $n+1/2$  can be found using (B1) and (B2) combined with

$$\begin{aligned} \mathbf{U}_j^{n+1/2} = & \frac{\mathbf{U}_{j+1/2}^n + \mathbf{U}_{j-1/2}^n}{2} \\ & + \frac{\Delta t}{2} \left( -\frac{\mathbf{R}_{j+1/2}^n - \mathbf{R}_{j-1/2}^n}{\Delta x} + \frac{\mathbf{S}_{j+1/2}^n + \mathbf{S}_{j-1/2}^n}{2} \right) \end{aligned}$$

for  $j = m+1/2$  and  $j = m-1/2$ .

### Discrete Boundary Conditions for the Large Arteries

In order to use the two-step Lax–Wendroff scheme at the boundaries, a boundary condition must be applied. This can be done by combining the boundary conditions with the Lax–Wendroff scheme (B3) and solving for  $q$  and  $A$ . Details follow for the different types of boundary conditions that we have to consider.

*Inflow Boundary Condition.* The inflow  $q$  into the aorta is given by the periodic function shown in Fig. 3. Inserting  $q$  into (B3) gives a nonlinear equation for  $A$ , which can

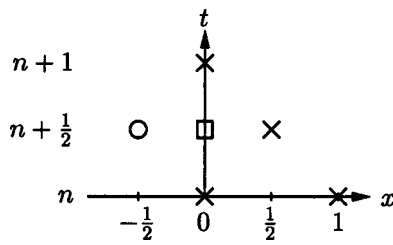


**FIGURE B2.** Left boundary: All variables are known at the points marked with a cross. In order to determine the value of  $A_0^{n+1}$ , we apply the boundary condition for  $q_0^{n+1/2}$  at the point marked with a square, and from taking the average of this point and the point at  $(1/2, n+1/2)$  it is possible to determine an approximate value at the ghost point marked with a circle. Finally,  $A_0^{n+1}$  can be found using this construction and the Lax–Wendroff scheme (B3).

be solved using Newton’s method. The Lax–Wendroff scheme (B3) requires evaluation of  $q_{-1/2}^{n+1/2}$  which, as shown in Fig. B2, can be found as follows

$$q_0^{n+1/2} = \frac{1}{2}(q_{-1/2}^{n+1/2} + q_{1/2}^{n+1/2}) \Leftrightarrow q_{-1/2}^{n+1/2} = 2q_0^{n+1/2} - q_{1/2}^{n+1/2}. \tag{B4}$$

*Outflow Boundary Conditions.* The outflow boundary condition for the large arteries should be evaluated at each of the terminal vessels (see Fig. 1), i.e., at  $x_L = M\Delta x$ , where  $x_L$  is the length of the vessel and  $M$  is the number of subintervals along the vessel. For any given terminal vessel the outflow boundary condition is determined by the convolution integral (38)

$$p(x_L, t) = \int_{t-T}^T q(x_L, t - \tau) z(x_L, \tau) d\tau,$$

which can be discretized by

$$p(M\Delta x, n\Delta t) = p_M^n = q_M^n y_M^0 \Delta t + \sum_{k=1}^{N-1} q_M^{(n-k)_N} z_M^k \Delta t, \tag{B5}$$

where  $t = n\Delta t$  is the current time,  $N$  is the number of timesteps per period, and  $\langle \cdot \rangle_N$  denotes the modulo operator, the range of which is the set  $\{0, 1, \dots, N-1\}$ . The sum in (B5) contains the terms from this and the previous period depending on the value of  $k$ , see Fig. B3.

Evaluating the outflow boundary condition is a bit subtle, since  $p(x_L, t)$  (and hence,  $A$ ) is not known explicitly, but only as a function of  $q$ . Consequently, inserting the outflow boundary condition (B5) into the Lax–Wendroff scheme (B3) gives rise to a system of nonlinear equations which can be solved using Newton’s method (for details see Olufsen).<sup>20</sup>

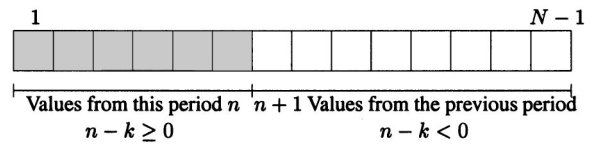


**FIGURE B3.** The discretized convolution integral (38) runs over a whole period. For a given time  $t = n\Delta t$  the values for  $p$  predicted from this period is used for  $k=1, \dots, n$  and the values predicted in the previous period for  $k=n+1, \dots, N-1$ .

*Bifurcation Conditions.* Bifurcations represent an outflow boundary for the parent vessel and an inflow boundary for the daughter vessels. In this case, the bifurcation conditions (16) and (18) must be combined with the Lax–Wendroff scheme (B3) to solve for  $q_M$  and  $A_M$ ,  $M=M$  for the parent vessel and  $M=0$  for the daughter vessels. As in the case of the inflow boundary condition, ghost points are introduced in order to get these estimates. As described in the section on Boundary Conditions for the Large Arteries, the case study presented in this paper use (18) for all bifurcations except for the bifurcation from the ascending aorta into anomya and the aortic arc. In the latter bifurcation the energy loss is substantial and (17) is used instead of (18). In the bifurcations using (16) and (18) together with the ghost points we can find  $(q_i)_M^{n+1/2}$  and  $(A_i)_M^{n+1/2}$ , where  $i = pa, d_1, d_2$ . Hence, the bifurcation conditions, at time-level  $n+1/2$  and  $n+1$ , lead to the following equations. Conservation of flow (16) across the bifurcation

$$(q_{pa})_M^j = (q_{d_1})_0^j + (q_{d_2})_0^j \tag{B6}$$

and the pressure condition (18)

$$(p_{d_i})_0^j = (p_{pa})_M^j, \tag{B7}$$

where  $i = 1, 2$  and  $j = n+1/2, n+1$ . The latter equation can be written in terms of  $A$  using the state Eq. (14):

$$(f_{d_i})_0 \left( 1 - \sqrt{\frac{(A_{d_i})_0}{(A_{d_i})_0^j}} \right) = (f_{pa})_M \left( 1 - \sqrt{\frac{(A_{0pa})_M}{(A_{pa})_M^j}} \right), \tag{B8}$$

where  $i = 1, 2$ ,  $j = n+1/2, n+1$ , and  $f(r_0) = 4Eh/(3r_0)$  represents the changing stiffness or compliance of the vessels. Note that if (17) is used instead of (18) Eqs. (B7) and (B8) should be modified accordingly.

As in the case of the large arteries, combining the bifurcation conditions (B6) and (B8) with the Lax–Wendroff scheme (B3) yields a number of nonlinear

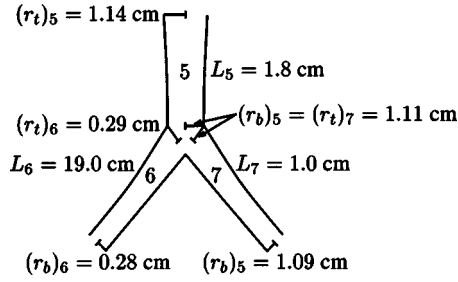


**FIGURE B4.** An arterial tree with three branches. For each branch its length, inlet and outlet diameters are specified. The example shown in this figure corresponds to the bifurcation from the aortic arc into the carotid artery and the descending aorta (from 5 into 6 and 7 on Fig. 1).

equations which can be solved using Newton's method (again, see Olufsen<sup>20</sup> for details).

#### Algorithms for the Large Arteries

In the case study presented in this paper the loss coefficients are set to zero, except in the bifurcation from the ascending aorta into the aortic arc and anomya. This has the advantage that all parameters specific to a given vessel can be specified locally. The parameters specified for each vessel are: length ( $L$ ), inlet radius ( $r_i$ ), outlet radius ( $r_b$ ), pointers to daughter vessels  $d_1$  and  $d_2$  ( $\text{art}[d_1]$  and  $\text{art}[d_2]$ ), radius at which the structured tree should be terminated ( $r_{\min}$ ), number of points per vessel ( $\#$ ), the vessel stiffness constants ( $k_1, k_2, k_3$ ), and loss coefficients ( $K_{d_1}, K_{d_2}$ ) where appropriate (as discussed earlier). Note, if the vessel has daughters, the parameter specifying the minimum radius should be zero. If the vessel is terminal, no pointers are needed for daughter vessels, but the parameter specifying the minimum radius must be set. For each vessel, the parameter values specific to the vessel will be specified when the tree is initialized. Algorithm 1 describes initialization of the arterial tree shown in Fig. B4 and algorithm 2 describes the solution to the hyperbolic equations in (6) and (13).

#### Algorithm 1: The Arterial Tree

- Number of vessels in the network ( $\text{nbrves}=3$ ).
- Starting time for the simulation ( $\text{tstart}=0$ ).
- Ending time for the simulation ( $\text{finaltime}=6$ ).
- initialization of the arterial tree ( $\text{art}=\text{new ves}*\text{[nbrves]}$ ).
- $\text{art}[3]=\text{new ves}[1.0,1.11,1.09,0,0, (r_{\min})_3,4,k_1, k_2, k_3,0,0]$ .
- $\text{art}[2]=\text{new ves}[19.0,0.29,0.28,0,0, (r_{\min})_2,4,k_1, k_2, k_3,0,0]$ .
- $\text{art}[1]=\text{new ves}(1.8,1.14,1.11,\text{art}[2],\text{art}[3], 0,4,k_1, k_2, k_3,0,0)$ .

The array "art" comprises information about the vessels shown in Fig. B4;  $\text{art}[3]$  comprise vessel 7,  $\text{art}[2]$  vessel 6, and  $\text{art}[1]$  vessel 5. The number of the vessels in Fig. B4 correspond to the numbers in the full arterial tree (see Fig. 1). However, since vessels 6 and 7 do not correspond to terminal vessels in the full arterial tree, we have left out values for the minimum radii and instead noted that a minimum radius must be provided at the appropriate location.

#### Algorithm 2: Solving the Equations for the Large Arteries

- While  $t < \text{finaltime}$   $[-1.125\text{cm}]$ 
  - For all vessels do  $[-0.75\text{cm}]$ 
    - Check that the CFL-condition applies.
    - Solve the equations for all interior points using the Lax–Wendroff scheme (B3).
    - Update the inlet boundary condition (B4) for the vessel connected to the heart ( $\text{art}[1]$ ).
    - Check if the vessel has daughters. Use the bifurcation conditions (B6) and (B8) if the vessel has daughters, otherwise the vessel is terminal and the outflow boundary condition (B5) should be used.

#### Algorithms for the Small Arteries

The recursive approach to compute the root impedances of the structured trees is described in algorithms 3 and 4. Assume that the number of timesteps  $N$ , a root radius ( $r_{\text{root}}$ ) and the minimum radius ( $r_{\min}$ ) has been given.

#### Algorithm 3: The Root Impedance $Z(0,\omega)$

- For each frequency determine  $Z(0,\omega)$  as follows: Compute the impedance for  $N$  values of  $\omega$ . Since  $Z$  is self-adjoint the impedance can be computed using the following two steps.
  - For  $k=N/2+1, N+1$  do
    - Let all previous computed results be reset to zero. Use the list "comp" to store temporary results such that it is not necessary to reevaluate identical parts of the structured tree.
    - Find  $Z(0,\omega)$  recursively using the function  $Z_0(\omega_k,0,0)$ , which is described in Algorithm 4.
  - Apply self-adjointness by

$$Z(0,\omega_k) = \overline{Z(0,\omega_{k+N/2})}$$

- Determine  $z(0,t)$  by inverse Fourier transform of  $Z(0,\omega)$ .

Algorithm 4: Recursive computation of  $Z_0(\omega_k, n_\alpha, n_\beta)$

- (1) Compute all parameters for the vessel and initialize the array ‘‘comp’’ to zero:
  - Radius  $r_0 = \alpha^{n_\alpha} \beta^{n_\beta} r_{\text{root}}$ .  
Note,  $n_\alpha$  and  $n_\beta$  correspond to specific values of  $k$  and  $n-k$  in Eq. (20); this new notation is more convenient for the present description.
  - Cross-sectional area  $A_0 = \pi r_0^2$ .  
This definition is similar to the one for the large arteries defined above Eq. (4).
  - Stiffness/compliance  $f(r_0) = 4Eh/(3r_0)$ .  
This factor is defined below Eq. (B8).
  - Vessel length  $L = r_0 l_{\text{tr}}$ .  
This factor is defined below Eq. (36).
- (2) Compute the wave-propagation velocity  $c$  (33) and the scalar  $g$  [defined above Eq. (34)]. These depend on  $F_J$  (27) and thus on the Womersley number  $w$  [defined below Eq. (25)].
- (3) Recursive algorithm:
  - If  $r_0 < r_{\text{min}}$  then
    - $Z_L(\omega_k, n_\alpha, n_\beta)$  = terminal resistance.
  - else
    - If the root impedance of the left daughter ( $n_\alpha + 1, n_\beta$ ) has been computed previously then
      - $Z_0(\omega_k, n_\alpha + 1, n_\beta) = \text{comp}(n_\alpha + 1, n_\beta)$ .
    - else
      - Compute the root impedance of the left daughter by calling  $Z_0(\omega_k, n_\alpha + 1, n_\beta)$  recursively.
      - If the root impedance of the right daughter ( $n_\alpha + 1, n_\beta$ ) has been computed previously then  $Z_0(\omega_k, n_\alpha, n_\beta + 1) = \text{comp}(n_\alpha, n_\beta + 1)$ .
      - else Compute the root impedance of the right daughter by calling  $Z_0(\omega_k, n_\alpha, n_\beta + 1)$  recursively.
  - $Z_L(\omega_k, n_\alpha, n_\beta) = 1/[Z_0^{-1}(\omega_k, n_\alpha + 1, n_\beta) + Z_0^{-1}(\omega_k, n_\alpha, n_\beta + 1)]$ , (37).
- (4) If  $\omega_k \neq 0$  then
  - $Z_0(\omega_k, n_\alpha, n_\beta) = \frac{ig^{-1} \sin(\omega L/c) + Z(L, \omega) \cos(\omega L/c)}{\cos(\omega L/c) + igZ(L, \omega) \sin(\omega L/c)}$ , (35).
- (5) else, if  $\omega_k = 0$  then
  - $Z_0(\omega_k, n_\alpha, n_\beta) = \frac{8\mu l_{rr}}{\pi r_0^3} + Z_L(\omega_k, n_\alpha, n_\beta)$ , (36).
- (6) Update the table of pre-computed values:
  - $\text{comp}(n_\alpha, n_\beta) = Z_0(\omega_k, n_\alpha, n_\beta)$ .

For all of our simulations the terminal resistance is taken to be zero and the impedance is predicted solely from the structured tree. However, it is easy to modify the algorithm to incorporate an additional terminal impedance beyond that provided by the tree itself.

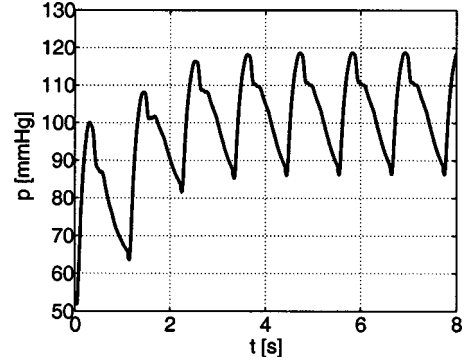


FIGURE B5. Aortic pressure 8 cm after the aortic valve. The plot shows that  $p(x, t)$  converges after about four periods.

Algorithms (3) and (4) only determine the frequency-dependent impedance, while the outflow boundary condition (38) for the large vessels require a time-dependent impedance. However, the response function  $z(0, t)$  and hence the impedance that appears in the convolution integral in (38) can be found by inverse Fourier transform of the root impedance  $Z(0, \omega)$ . The convolution spans one period, hence, knowledge of the solution at all timesteps during that period is required. Since Eqs. (6) and (13) are solved using the explicit two-step Lax–Wendroff method, the solution is not simultaneously available at all times during the period. Because we assumed that propagation of the flow and pressure waves is periodic this difficulty can be overcome using an iterative approach. At any time  $t$  values from the previous period (for  $t' \in [t: T]$ ) are used together with the ones already available for  $t' \in [0: t]$  (see Fig. B3). Iteration is carried out over a number of periods until a stable solution is reached. Experiments suggest that a stable solution is reached after about four periods (see Fig. B5). Another possibility would be to investigate whether the equations can be solved using a self-similar approach. This does not seem to be possible because of the viscous treatment of the momentum equation and the manner in which the tree is terminated when a fixed radius is reached. We have, however, been able to solve for the input impedance of an inviscid, infinite, self-similar tree (for details see Olufsen).<sup>20</sup>

## ACKNOWLEDGMENTS

This research was made possible by the Group Infrastructure Grant No. DMS-9631755 from the National Science Foundation and by the Danish Eureka Project No. 1063.

## REFERENCES

- <sup>1</sup>Anliker, M., R. L. Rockwell, and E. Ogden. Nonlinear analysis of flow pulses and shock waves in arteries. *Z. Angew. Math. Phys.* 22:217–246, 1971.
- <sup>2</sup>Atabek, H. B. Wave propagation through a viscous fluid contained in a tethered, initially stressed, orthotropic elastic tube. *Biophys. J.* 8:626–649, 1968.
- <sup>3</sup>Avolio, A. Aging and wave reflection. *J. Hypertens.* 10:S83–S86, 1992.
- <sup>4</sup>Barnard, A. C. L., W. A. Hunt, W. P. Timlake, and E. Varley. A theory of fluid flow in compliant tubes. *Biophys. J.* 6:717–724, 1966.
- <sup>5</sup>Bassingthwaite, J. B., L. S. Liebovitch, and B. J. West. *Fractal Physiology*. The American Physiological Society Methods in Physiology Series. New York: Oxford University Press, 1994, pp. 236–262.
- <sup>6</sup>Caro, C. G., T. J. Pedley, R. C. Schroter, and W. A. Seed. *The Mechanics of the Circulation*. Oxford: Oxford University Press, 1978, pp. 151–433.
- <sup>7</sup>Chorin, A. J., and J. E. Marsden. *A Mathematical Introduction to Fluid Mechanics*. 3rd ed. New York: Springer 1998, pp. 1–46.
- <sup>8</sup>Courant, R., K. Friedrichs, and H. Lewy. Über die partiellen differenzgleichungen de mathematischen physic. *Math. Ann.* 100:32–74, 1928.
- <sup>9</sup>Feinberg, A. W., and H. Lax. Studies of the arterial pulse wave. *Circulation* 18:1125–1130, 1958.
- <sup>10</sup>Guyton, A. C. *Textbook of Medical Physiology*, 9th ed. Philadelphia: W. B. Saunders Company, 1996, pp. 161–294.
- <sup>11</sup>Iberall, A. S.. Anatomy and steady flow characteristics of the arterial system with an introduction to its pulsatile characteristics. *Math. Biosci.* 1:375–385, 1967.
- <sup>12</sup>Janna, W. S. *Introduction to Fluid Mechanics*, 3rd ed. Boston: PWS-Kent, 1993.
- <sup>13</sup>Kannel, W. B., P. A. Wolf, D. L. McGee, T. R. Dawber, P. McNamara, and W. P. Castelli. Systolic blood pressure, arterial rigidity, and risk of stroke. *J. Am. Med. Assoc.* 245:1225–1229, 1981.
- <sup>14</sup>Kassab, G. S., C. A. Rider, N. J. Tang, and Y. C. Fung. Morphometry of Pig Coronary Arterial Trees. *Am. J. Physiol.* 265:H350–H365, 1993.
- <sup>15</sup>Kozerke, S., R. Botnar, S. Oyre, M. B. Scheidegger, E. M. Pedersen, and P. Boesiger. Automatic vessel segmentation using active contours in cine phase contrast flow measurements. *J. Magn. Reson. Imaging.* 10:41–51, 1999.
- <sup>16</sup>Lax, H., A. Feinberg, and B. M. Cohen. The normal pulse wave and its modification in the presence of human atherosclerosis. *J. Chronic. Dis.* 3:618–631, 1956.
- <sup>17</sup>Lighthill, J. *Mathematical Biofluidynamics*. 3rd ed. Philadelphia: Society for Industrial and Applied Mathematics, 1989, pp. 227–253.
- <sup>18</sup>Murray, C. D. The physiological principle of minimum work applied to the angle of branching of arteries. *Am. J. Physiol.* 9:835–841, 1926.
- <sup>19</sup>Nichols, W. W., and M. F. O'Rourke. *McDonald's Blood Flow in Arteries*, 4th ed. London: Edward Arnold, 1998, p. 564.
- <sup>20</sup>Olufsen, M. PhD thesis. Modeling the arterial system with reference to an anesthesia simulator. Roskilde: IMFUFA, Roskilde University, Denmark. Text No 345, 1998.
- <sup>21</sup>Olufsen, M. Structured tree outflow condition for blood flow in larger systemic arteries. *Am. J. Physiol.* 276:H257–H268, 1999.
- <sup>22</sup>Papageorgiou, G. L., B. N. Jones, V. J. Redding, and N. Hudson. The area ratio of normal arterial junctions and its implications in pulse wave reflections. *Cardiovasc. Res.* 24:478–484, 1990.
- <sup>23</sup>Pedersen, E. M., H.-W. Sung, A. C. Burlson, and A. P. Yoganathan. Two-dimensional velocity measurements in a pulsatile flow model of the abdominal aorta simulating different hemodynamic conditions. *J. Biomech.* 26:1237–1247, 1993.
- <sup>24</sup>Pedley, T. J. *The Fluid Mechanics of Large Blood Vessels*. Cambridge: Cambridge University Press, 1980, pp. 1–159.
- <sup>25</sup>Peskin, C. S. *Partial Differential Equations in Biology*. New York: Courant Institute of Mathematical Sciences, New York University, 1976, pp. 160–208.
- <sup>26</sup>Pollanen, M. S. Dimensional optimization at different levels at the arterial hierarchy. *J. Theor. Biol.* 159:267–270, 1992.
- <sup>27</sup>Segers, P., F. Dubois, D. DeWachter, and P. Verdonck. Role and relevancy of a cardiovascular simulator. *Cardiovasc. Eng.* 3:48–56, 1998.
- <sup>28</sup>Stergiopoulos, N., D. F. Young, and T. R. Rogge. Computer simulation of arterial flow with applications to arterial and aortic stenosis. *J. Biomech.* 25:1477–1488, 1992.
- <sup>29</sup>Tardy, Y., J. J. Meiseter, F. Perret, H. R. Brunner, and M. Arditi. Non-invasive estimate of the mechanical properties of peripheral arteries from ultrasonic and photoplethysmographic measurements. *Clin. Phys. Physiol. Meas.* 12:39–54, 1991.
- <sup>30</sup>Uylings, H. B. M. Optimization of diameters and bifurcation angles in lung and vascular tree structures. *Bull. Math. Biol.* 39:509–520, 1977.
- <sup>31</sup>Westerhof, N., F. Bosman, C. J. DeVries, and A. Noordergraaf. Analog studies of the human systemic arterial tree. *J. Biomech.* 2:121–143, 1969.
- <sup>32</sup>Womersley, J. R. An elastic tube theory of pulse transmission and oscillatory flow in mammalian arteries. Technical Report WADC TR:56–614, Wright Air Development Center (WADC), Air Research and Development Command, United States Air Force, Wright-Patterson Air Force Base, Ohio, 1957.
- <sup>33</sup>Young, D. F., and F. Y. Tsai. Flow characteristics in models of arterial stenosis - ii. unsteady flow. *J. Biomech.* 6:547–559, 1973.
- <sup>34</sup>Zamir, M. Nonsymmetrical bifurcations in arterial branching. *J. Gen. Physiol.* 72:837–845, 1978.